

Nonlinear optical spectra from Rydberg-mediated photon-photon interactions

Xinghan Wang,¹ Yupeng Wang,¹ Aishik Panja,¹ and Qi-Yu Liang^{1,2}

¹*Department of Physics and Astronomy, Purdue University, West Lafayette, IN 47907, USA*

²*Purdue Quantum Science and Engineering Institute,
Purdue University, West Lafayette, IN 47907, USA*

(Dated: February 13, 2026)

While RydbergRydberg interactions are essential for quantum nonlinear optics and quantum information processing, their role in microwave and radio-frequency sensing remains poorly understood. Here we experimentally investigate Rydberg interaction-induced nonlinearity in cold-atom Rydberg electromagnetically induced transparency (EIT). In a three-level EIT system, increasing photon-photon interactions produces nonlinear spectral broadening accompanied by resonance shifts, while a microwave-dressed four-level system exhibits pronounced nonlinear broadening without detectable spectral shifts. Our three-level data can be explained by a conditional superatom model, whereas our four-level observations are surprisingly captured by a simple dephasing model. Comparisons with three representative models provide key insights to the role of many-body interactions in Rydberg EIT spectroscopy. Furthermore, our results clarify the conditions under which microwave field characterization can be performed in the nonlinear regime without introducing systematic bias. Our study advances both fundamental understanding of many-body physics and practical development of atomic sensors.

Rydberg atoms provide a uniquely versatile platform for engineering strong, tunable interactions in otherwise weakly interacting neutral-atom systems. They couple strongly to each other and to external fields. The former enables controllable atom-atom, atom-photon and even photon-photon interactions. Strong atom-atom interactions have established atom arrays as a leading platform for quantum information processing and quantum simulation [1–4], while atom-photon and Rydberg-mediated effective photon-photon interactions lead to breakthroughs in quantum optics [5–7] and underpin a broad range of optical quantum technologies, such as on-demand single-photon sources [8], deterministic photonic entangling gates [9, 10], non-classical photonic state generation [11], distributed quantum computing [12] and quantum networking [13]. In the latter case, strong coupling to external fields promises exceptionally sensitive and broadband microwave (MW) and radio frequency (RF) sensing capabilities [14–16]. Rydberg sensors span over six orders of magnitude in frequency, from below one megahertz to terahertz range [6, 17], and provide International System of Units (SI) traceable, self-calibrated measurements.

Although the vast majority of MW/RF sensors employ vapor cells, laser-cooled atoms have drawn increasing attention in recent years. Cold atomic systems significantly suppress Doppler broadening that limits vapor cell sensitivity, offering a path towards quantum-limited performances [18–22]. Beyond improved performance in traditional sensing schemes, cold atoms open up new approaches, such as leveraging quantum entanglement [23, 24], coherence [25], and avalanche gain [26, 27].

However, the role of Rydberg-Rydberg interactions in MW/RF sensing remains vastly underexplored. While these interactions are essential for quantum information processing applications, in sensing contexts they could introduce resonance shifts that lead to systematic er-

rors, and increased decoherence that broadens spectral features. Sensing signals are typically optically read out through electromagnetically induced transparency (EIT). While interaction effects on the resulting transmission spectra are likely to be more pronounced in cold-atom systems, their role in vapor-cell sensors also remains uncharacterized. This gap calls for a deeper understanding of how underlying atomic interactions impact the prospects and limitations of atomic sensors.

Beyond these practical sensing considerations, from a fundamental-physics perspective, it is important to understand how many-body interactions modify the EIT response. At low photon-rate limit, the nonlinear effect can be well captured by an effective field theory [28]. However, this method is intractable at high photon rates, reflecting the broader challenge of describing strongly interacting many-body systems. To grasp the core physics, we first consider a three-level EIT system without MW/RF coupling. From a mean-field perspective, since van der Waals interactions, characterized by a C_6 coefficient, produce level shifts with a definite sign, the resulting spectra are expected to show resonance shifts following the sign of the underlying C_6 interaction. However, early experimental observations [29, 30] contradict this picture; the nonlinearity appeared as lowered resonance peak heights, while no appreciable shifts were reported. As such, a model [31] that accounts for interaction saturation within a blockade radius was introduced and shown to capture the main observed features; however, it still predicts a resonance shift that was not observed experimentally. As a result, the existing work remains insufficient to establish consensus in the field and does not address the consequences of Rydberg-Rydberg interactions in the presence of MW/RF driving.

Here, we experimentally explore the impact of atomic interactions in (MW-dressed) cold-atom Rydberg EIT. First, we apply probe and control laser fields in a three-

level system without MW driving. As the photon-photon interaction is increased by raising the probe photon rate, we observe spectral peak broadening similar to prior studies [29, 30]. At the same time, we observe a resonance shift that was not reported in these works and is consistent with the predictions of the model mentioned above. Next, we introduce MW driving in the presence of a large bias magnetic field to spectrally separate Zeeman sublevels, thereby isolating an effective four-level system. In this case, we do not observe appreciable spectral shifts when nonlinear broadening becomes comparable to the three-level case where shifts occur. We compare three representative models currently used in the literature to describe the nonlinearity arising from Rydberg-mediated photon-photon interactions. These models predict qualitatively distinct spectral features: one predicts both peak shifts and broadening, another predicts only shifts, and the third predicts only broadening. This qualitative distinction allows us to make meaningful comparisons with our data at the level of characteristic spectral features, rather than detailed parameter choices.

RESULTS

Experimental setup and procedure

We perform Rydberg EIT in a spin-polarized cloud of ^{87}Rb atoms. The atoms are initially prepared in the ground state $|1\rangle = |5S_{1/2}, F=2, m_F=-2\rangle$, where F and m_F denote the hyperfine and magnetic sublevels, respectively. A weak σ^- -polarized probe laser couples the ground state to an intermediate state $|2\rangle = |5P_{3/2}, F=3, m_F=-3\rangle$, which is coupled to a Rydberg state $|3\rangle = |3_{-1/2}\rangle = |61S_{1/2}, m_j=-1/2\rangle$ via a σ^+ -polarized control laser (Fig. 1(a)). Additionally, a MW field addresses the $|3\rangle \leftrightarrow |4\rangle = |4_{m_j}\rangle = |61P_{3/2}, m_j\rangle$ transition. Here, j and m_j denote the total angular momentum quantum numbers and the projection of the latter along the quantization axis, respectively.

The atoms are laser-cooled in a magneto-optical trap and transferred to a far-detuned 1064 nm optical dipole trap, following the procedure described in Ref. [32]. We apply a bias magnetic field $B = 3.7$ G along the probe propagation direction to define the quantization axis and perform optical pumping. The dipole-trapped atomic cloud has a temperature of $14 \mu\text{K}$ achieved via gray molasses. Doppler broadening is further reduced by applying counter-propagating 780 nm probe and 479 nm control beams. The atomic cloud has a root-mean-square (RMS) radius of $10 \mu\text{m}$ along the probe propagation direction and an optical depth (OD) of approximately 0.4.

We modulate the dipole trap with a period of $180 \mu\text{s}$ and 50% duty cycle, and probe during the dipole-trap-off time. After 50 modulation cycles, we keep the dipole trap off to allow the atoms to disperse. Following a 10 ms time-of-flight, we probe for 2 ms to measure counts without atoms. We average these no-atom counts to obtain a single normalization factor for each spectroscopy scan, which is used to normalize the transmission data. We then average the normalized probe transmission over

multiple scans. Each spectral data point corresponds to roughly 20 ms of interrogation time. We infer the probe photon rate R_p at the apparatus from the no-atom counts, accounting for the collection and the single photon counting module's (SPCM-AQRH-14-FC) detection efficiency.

The MW fields are delivered by a broadband horn antenna (FMWAN159-10SF, Fairview Microwave) driven by a signal generator (Anritsu 68369A/NV). Despite using a single antenna, the MW field at the atoms contains all σ^+ , σ^- and π polarization components due to reflections and scattering from the in-vacuo components, the vacuum chamber and nearby external structures, as is typical in cold-atom experiments [33].

Physical model

We consider three representative models to account for the nonlinearity arising from Rydberg-Rydberg interactions. All models share the concept of superatoms (SAs); namely, all atoms within a blockaded volume $V_b = \frac{4\pi}{3} R_b^3$ collectively behave like a single atom, because the interaction shifts multiple Rydberg excitations out of resonance, preventing doubly- or higher-excited states. Here, R_b denotes the blockade radius and is defined through $C_6^{33}/R_b^6 = \Omega_c^2/(2\Gamma_2)$, where C_6^{33} is the van der Waals coefficient of the Rydberg state $|3_{-1/2}\rangle$, Ω_c is the control Rabi frequency, and $\Gamma_2/(2\pi) = 6.1$ MHz is the spontaneous decay rate of the intermediate state $|2\rangle$. These models enforce the blockade condition by restricting the allowed basis states to the ground and singly-excited manifold within each SA.

Detailed descriptions of the models are provided in "Methods: Model descriptions". Here, we outline the key concepts. In the *conditional model* [31], we spatially coarse-grain the atomic cloud with each pixel corresponding to an SA. The polarizability is determined by two mutually exclusive conditions: if the SA contains a Rydberg excitation, then the polarizability would be the same as that of the system in the absence of control coupling, representing the saturation of interaction (blockade); if the SA is not excited, then atoms outside the SA contribute to a mean-field shift, resulting in a polarizability with a modified control detuning. To implement this model numerically, we consider a 1D SA chain and divide the propagation length L into $L/(2R_b)$ intervals. At each step, we perform Monte Carlo sampling for Rydberg excitation, and evaluate probe field intensity correlation function $g^{(2)}(z)$ and probe Rabi frequency $\Omega_p(z)$ accordingly. The probe transmission T is modeled by averaging $\left| \frac{\Omega_p(z=L)}{\Omega_p(z=0)} \right|^2$ over 50 independent realizations.

Extending this model from the original three-level system to four-level systems requires carefully generalizing the conditional structure of the model in the presence of three interactions with different strengths, characterized by the van der Waals coefficients C_6^{33} and C_6^{44} for $|3\rangle - |3\rangle$ and $|4\rangle - |4\rangle$ interactions, and the dipole-dipole coefficient C_3^{34} for $|3\rangle - |4\rangle$ interactions. In this case, the number and form of the conditioning branches, as well as the as-

sociated mean-field contributions, must be reformulated and depend on the hierarchy of the interaction strengths. We leave the extension of this model to a four-level system to future work and focus instead on contrasting these conceptually distinct models.

In the *unconditional model* [34], we do not distinguish whether an SA is excited or not, instead calculating the polarizability exclusively with a modified control detuning arising from a mean-field shift. The original work suggests integrating the interaction starting from the interatomic distance to obtain the mean-field results. This leads to very large spectral peak shifts which we do not observe in either our three-level or our four-level systems. To be consistent with other models and the SA framework, we instead set the lower limit to be R_b , reflecting that only external SAs outside the blockade volume contribute to the mean-field interactions.

When applied to the four-level system, the mean-field interactions modify the detunings and MW Rabi frequency as $\delta_2 \rightarrow \delta_2 - s_{33} - s_{34}$, $\delta_3 \rightarrow \delta_3 - s_{44} - s_{43}$ and $\Omega_m \rightarrow \Omega_m + 2e_{34}$. Here, s_{33} and s_{44} denote the level shifts originating from C_6^{33} and C_6^{44} , respectively. Our level $|3\rangle|4\rangle$ interaction exhibits both shift and splitting contributions. Therefore, we fit the pair interaction to the form $C_6^{34}/R^6 \pm C_3^{34}/R^3$ ("Methods: Interaction coefficients"). The C_6^{34} term induces shifts s_{34} for level $|3\rangle$ and s_{43} for level $|4\rangle$. The C_3^{34} term contributes to exchange interaction e_{34} . $\delta_2 = \Delta_p + \Delta_c$ is the two-photon detuning, $\delta_3 = \Delta_p + \Delta_c + \Delta_m$ is the three-photon detuning, Ω_m is the MW Rabi frequency, and Δ_p , Δ_c and Δ_m are probe, control and MW detunings.

Finally, in the *dephasing model* [18], we treat the variance of the mean-field interactions as an additional dephasing mechanism, incorporating it as increased Rydberg decoherence rates, rather than modifying the detunings and MW Rabi frequency in the polarizability. Specifically, we modify the jump operators $L_k = \sqrt{\Gamma_k} |k\rangle \langle k|$ in the Lindbladian by replacing $\Gamma_3 \rightarrow \Gamma_3 + \sqrt{\text{Var}_{33}} + \sqrt{\text{Var}_{34}^s} + \sqrt{\text{Var}_{34}^e}$ and $\Gamma_4 \rightarrow \Gamma_4 + \sqrt{\text{Var}_{44}} + \sqrt{\text{Var}_{43}^s} + \sqrt{\text{Var}_{34}^e}$, where Var_{33} , Var_{44} , Var_{34}^s , Var_{43}^s and Var_{34}^e are the variances associated with s_{33} , s_{44} , s_{34} , s_{43} and e_{34} , respectively.

For all models, the probe-transition coherence ρ_{21} is calculated from the master equation

$$\dot{\rho} = \frac{i}{\hbar} [\rho, H] - \sum_k \frac{1}{2} \left(L_k^\dagger L_k \rho + \rho L_k^\dagger L_k - 2 L_k \rho L_k^\dagger \right) \quad (1)$$

with

$$H = \hbar \left(-\Delta_p |2\rangle \langle 2| - \delta_2 |3\rangle \langle 3| - \delta_3 |4\rangle \langle 4| + \frac{\Omega_p}{2} |1\rangle \langle 2| + \frac{\Omega_c}{2} |2\rangle \langle 3| + \frac{\Omega_m}{2} |3\rangle \langle 4| + \text{h.c.} \right) \quad (2)$$

$L_2 = \sqrt{\Gamma_2} |1\rangle \langle 2|$, together with $L_k = \sqrt{\Gamma_k} |k\rangle \langle k|$, $k \in \{3, 4\}$, are the only Lindbladian terms considered. Both the $61\text{S}_{1/2}$ and $61\text{P}_{3/2}$ Rydberg states have lifetime longer than $100 \mu\text{s}$ at room temperature, resulting

in negligible decay rates compared to other decoherence processes.

The steady-state solution of the density matrix ρ is associated with the probe transmission T via:

$$T = \exp \left[\text{OD} \text{Im}(\rho_{21}) \frac{\Gamma_2}{\Omega_p} \right] \quad (3)$$

Although Ω_p explicitly appears in the equation, the spectra exhibit virtually no dependence on Ω_p in the absence of Rydberg-Rydberg interaction and in the weak-probe limit with respect to single-atom saturation. In this case, the steady-state solution for ρ_{21} is proportional to Ω_p , which cancels out in the normalized probe transmission. For the probe Rabi frequency relevant to our experiments, we operate in this weak-probe limit. Therefore, the observed spectral dependence on Ω_p arises from Rydberg-mediated nonlinearity, rather than from single-atom EIT physics.

Nonlinearity in a three-level system

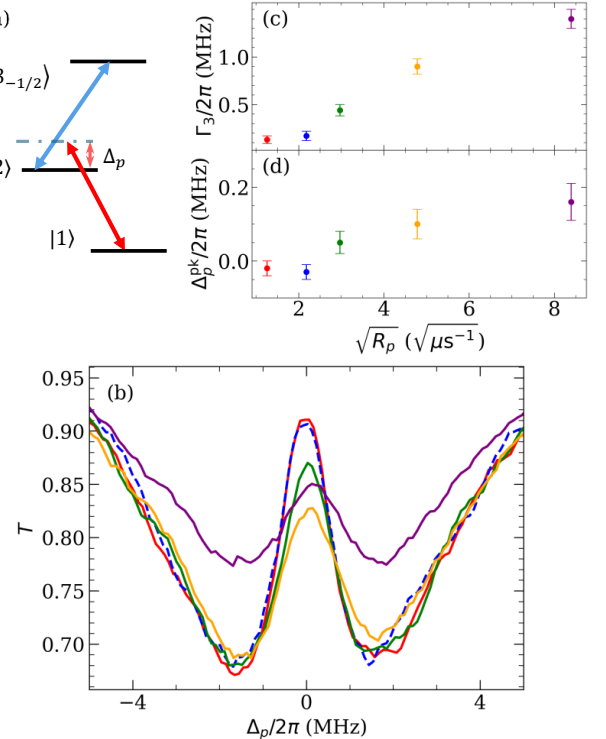


FIG. 1. Nonlinearity in a three-level system. (a) Level scheme. (b) Measured EIT spectra vs probe detuning. For clarity, we smooth the data using a moving average of window size 9 (see Fig. 2 for the raw data). The probe rate is $R_p = \{1.6, 4.8, 8.8, 22.9, 70.5\} \mu\text{s}^{-1}$ for the {red, blue, green, orange, purple} colors. This color coding is kept the same as in panel (c,d). (c) Γ_3 is extracted by fitting the linear model to the raw data. (d) The peak position Δ_p^{pk} is determined by Gaussian fits to the raw data in the central region.

The contribution from nonlinear interactions can be systematically varied by the atomic density and the

probe Rabi frequency. Increasing the atomic density, and thereby the atom number within a fixed atom-photon interaction volume, improves the signal-to-noise ratio by reducing atomic shot noise, while increasing the probe power reduces photonic shot noise; however, both enhancements also increase nonlinear interactions. This raises the question whether sensing can be performed in the presence of nonlinear effects and whether such effects introduce systematic errors.

We first investigate a three-level EIT system without MW coupling. As we increase the probe photon rate, the dominant effect is resonant peak height reduction (Fig. 1(b)), consistent with prior experimental studies [29, 30]. To quantify this phenomenon, we fit the *linear model* (Eqs. 1 and 2 with no interaction-induced substitutions and $\Omega_m = 0$) to the data (See "Methods: Spectral fits" for details of the parameters) and plot the fitted Γ_3 values vs the square root of the probe rate (Fig. 1(c)). At the lowest two rates, the effects of Rydberg-Rydberg interactions are negligible, with Γ_3 showing no rate dependence. As the rate further increases, Γ_3 increases. We attribute the OD reduction at the highest rate to atom loss from the probing region due to momentum kicks.

Importantly, we observe a resonant blue shift up to 0.2 MHz (Fig. 1(d)) along with peak height reduction, which increases with probe rate similarly to Γ_3 . This shift is expected from the mean-field perspective, in which the Rydberg interaction between S-state atoms shifts the level upward, resulting in a smaller effective two-photon detuning, thereby blue-shifting the resonant peaks. To ensure that the observed shift is not caused by uncontrolled parameters, we acquire spectroscopic data at different probe Rabi frequencies in randomized order and repeat the entire acquisition sequence multiple times using newly randomized orders.

To compare our data with the three models, we integrate the interaction contribution from R_b to infinity. Because the van der Waals interaction decays rapidly with distance, the precise choice of the upper integration limit is insignificant. We approximate our medium as homogeneous with an atomic number density of $\varrho = 2 \times 10^{10} \text{ cm}^{-3}$ and a length of $L = 64.8 \mu\text{m}$ such that $L/(2R_b) = 4$ is an integer for the Monte Carlo simulation. This length L roughly corresponds to 2.5 times the Gaussian effective length ($\sqrt{2\pi} \times \text{RMS length}$) extracted from absorption imaging. The remaining input parameters to these models are set to the fitted values of the linear model obtained from fits to the lowest-rate data. In the conditional and dephasing model, we include a baseline Rydberg dephasing rate $\Gamma_3/(2\pi) = 20 \text{ kHz}$, roughly accounting for Doppler broadening and ambient electric-field inhomogeneity. In the conditional model, this is the total dephasing rate, whereas in the dephasing model it serves as a background to which interaction-induced dephasing is added. In the unconditional model, $\Gamma_3/(2\pi)$ is empirically set to 200 kHz such that the model prediction is consistent with our measurement at the lowest rate.

As shown in Fig. 2, the unconditional model only pre-

dicts peak shifts, the dephasing model only predicts peak height reduction, whereas the conditional model predicts both. Only the conditional model adequately explains our observations. Note that although both the conditional and dephasing model predict peak height reduction, the underlying mechanisms differ starkly. In the conditional model, the peak height reduction arises from stochastic conditioning of the response. When a Rydberg excitation is present, the response is projected onto a no-control form, thereby making no contribution to the resonant peak at that step of the Monte Carlo sampling. Otherwise, it remains close to the usual EIT behavior with a small interaction shift. In contrast, in the dephasing model, the origin of dephasing lies in the random spatial distribution of atoms: atoms at different separations induce different interaction strengths, which introduces a distribution of level shifts and thus dephases the collective response. If the atoms are instead arranged in a lattice structure with well-defined spacings, this positional randomness would be strongly suppressed, and the corresponding dephasing would be minimal.

Nonlinearity in a four-level MW EIT system

In the presence of MW, we apply a large magnetic field $B = 15.7 \text{ G}$ and a sufficiently weak MW field, resonant with the Zeeman-shifted σ^+ transition, such that only a single Zeeman level, $|4_{1/2}\rangle$, is mixed with $|3_{-1/2}\rangle$ (Fig. 3(a)), thereby isolating a four-level subsystem. This configuration provides a classic level structure for SI-traceable, self-calibrated MW measurements. When scanning the control detuning Δ_c , while keeping the probe and MW fields on resonance, two resonant peaks arise from the probe absorption baseline. In such measurements, the splitting of the peaks, dubbed Autler-Townes (AT) splitting (Δ_{AT}), is proportional to the electric field amplitude of the MW (E_m) through Planck's constant (\hbar) and the dipole moment of the Rydberg transition (\wp_{34}):

$$E_m = \frac{\hbar}{\wp_{34}} \Delta_{\text{AT}} \quad (4)$$

Here, we are interested in how Rydberg-mediated nonlinearity affects this splitting and the spectra.

As illustrated in Fig. 3, the peak height reduction sets in clearly at a lower probe rate than in the three-level system. We do not observe any spectral peak shift as a function of probe rate, even though the Rydberg dephasing effect is evident. As a result, the nonlinear spectra can be used for MW detection at the cost of peak broadening.

The MW field electric field amplitude obtained from the Gaussian-fitted peak positions (Fig. 3(c,d)) is $1.30(2) \text{ mV/cm}$, corresponding to a Rabi frequency $\Omega_m/(2\pi) = 2.11(4) \text{ MHz}$. Alternatively, we can extract these values by fitting the linear model (Eqs. 1 and 2 with no interaction-induced substitutions). For instance, the fit results of the data in Fig. 3(e) are $\{\Delta_m, \Omega_m, \Omega_c, \Gamma_3, \Gamma_4\}/(2\pi) =$

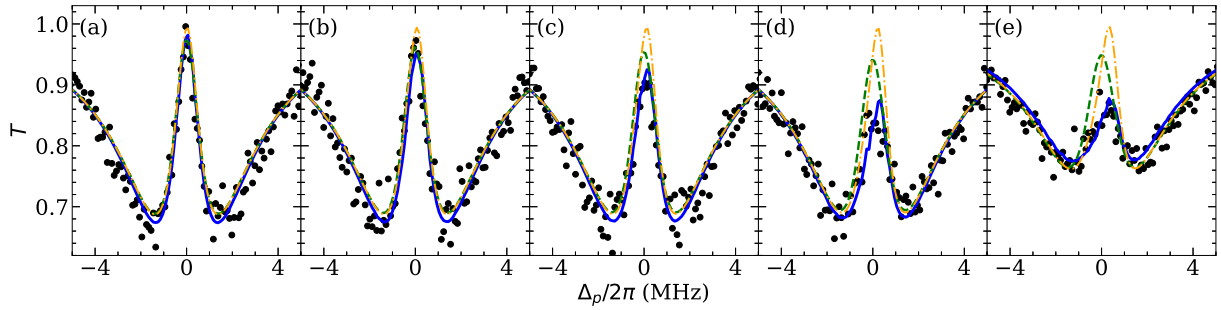


FIG. 2. Comparison of the three models (conditional model: blue solid line; dephasing model: green dashed line; unconditional model: orange dot-dashed line) with our three-level EIT data (same dataset as in Fig. 1, shown as black dots). Panels (ae) correspond to increasing probe rate.

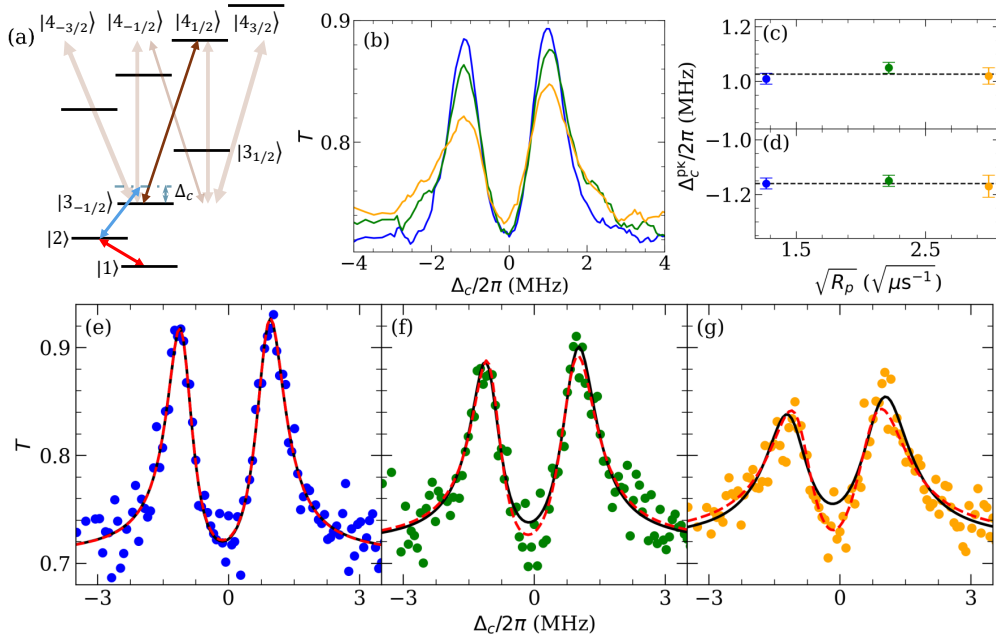


FIG. 3. Nonlinearity in a four-level system. (a) Level scheme. (b) Measured MW EIT spectra vs control detuning. For clarity, we smooth the data using a moving average of window size 9 (see the dots in panel (e-g) for the raw data). The probe rate is $R_p = \{1.6, 4.9, 8.9\} \mu\text{s}^{-1}$ for the {blue, green, orange} colors. The slight imbalance between the two peaks results from a small MW detuning $\Delta_m/(2\pi) = 0.15 \text{ MHz}$, which does not affect the extracted values of Ω_m within statistical uncertainties. The peak positions Δ_c^{pk} of the right and left peaks are determined by Gaussian fits to the raw data in the vicinity of each peak and plotted in panel (c) and (d). In panels (e-g), the red dashed and black solid lines are fit results from the linear model. The red dashed lines have independent Γ_3 and Γ_4 , with fitted values $\Gamma_3/(2\pi) = \{0.17(8), 0.6(1), 1.3(1)\} \text{ MHz}$ and $\Gamma_4/(2\pi) = \{0.21(7), 0.11(8), 0.10(9)\} \text{ MHz}$. The black solid lines enforce $\Gamma_3 = \Gamma_4$, with fitted values $\Gamma_{3,4}/(2\pi) = \{0.19(2), 0.32(3), 0.68(5)\} \text{ MHz}$.

$\{0.15(6), 2.04(2), 2.76(6), 0.17(8), 0.21(7)\} \text{ MHz}$ and $\text{OD} = 0.347(4)$. This Ω_m is 3% smaller than the value from the AT splitting. In fact, Ω_m obtained in this manner is systematically smaller than those extracted from the AT splitting. This discrepancy is likely caused by insufficient splitting of the peaks as compared to their widths (see Supplementary Part 1 and Ref. [35]). When the two peaks are relatively close, the lineshape is skewed, with the inner edges sharper than the outer edges. As such, the peak splitting does not perfectly match the MW Rabi frequency Ω_m . This behavior is tied to underlying EIT

response rather than a simple peak-overlap effect. Consequently, alternative peak-finding methods, such as double Gaussian fits, do not remedy this discrepancy.

The distortion of the lineshape does not solely depend on the peak splitting relative to the peak width; Γ_3 and Γ_4 contribute to the lineshape in distinct ways. Increasing Γ_4 raises the probe transmission between the two resonant peaks. However, as we increase the probe rate, the experimental transmission near $\Delta_c = 0$ remains low. Consequently, fitting the linear model consistently returns a small Γ_4 , even showing a trend of

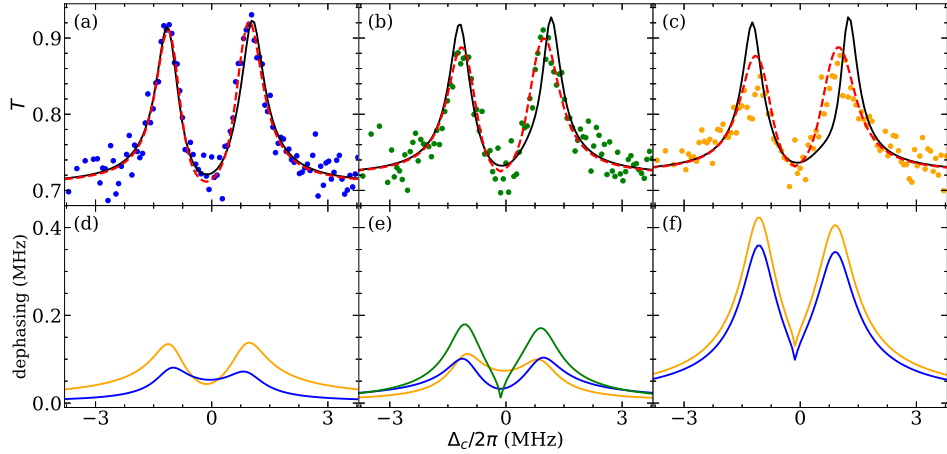


FIG. 4. Comparison of the unconditional model (black solid lines) and the dephasing model (red dashed lines) with our four-level MW EIT data (same dataset as in Fig. 3, shown as dots.) Panel (d-f) show interaction-induced Rydberg dephasing in the dephasing model for the highest probe rate $R_p = 8.9 \mu\text{s}^{-1}$, used for the red dashed curve in panel (c). (d) Contribution from the C_6^{33} ($\sqrt{\text{Var}_{33}}/(2\pi)$, orange) and C_6^{44} ($\sqrt{\text{Var}_{44}}/(2\pi)$, blue) terms. (e) Contribution from the C_6^{34} term to level $|3\rangle$ ($\sqrt{\text{Var}_{34}^s}/(2\pi)$, orange), from the C_6^{34} term to level $|4\rangle$ ($\sqrt{\text{Var}_{43}^s}/(2\pi)$, blue) and from the C_6^{34} term to both level $|3\rangle$ and $|4\rangle$ ($\sqrt{\text{Var}_{34}^s}/(2\pi)$, green). (f) Total interaction-induced Rydberg dephasing for level $|3\rangle$ (orange) and $|4\rangle$ (blue).

decreasing Γ_4 as the probe rate increases. This trend is opposite to physical expectations, and the resulting large Γ_3 also suppresses the peak-height imbalance that is clearly visible in the data. These spectral effects become evident by comparing two fitting approaches: one allowing Γ_3 and Γ_4 to vary independently (red dashed lines in Fig. 3(e-g)), and one constraining them to be equal (black solid lines in Fig. 3(e-g)). At high probe rates, allowing Γ_4 to vary freely forces it to smaller values to remain consistent with the low probe transmission near $\Delta_c = 0$, whereas constraining $\Gamma_4 = \Gamma_3$ fails to reproduce this feature. These behaviors signal a limitation of the linear model with probe-rate-dependent Rydberg decoherence. Nevertheless, both fitting approaches yield statistically identical MW Rabi frequencies until nonlinearity-induced $\Gamma_{3,4}$ significantly broaden the EIT linewidth ($\Gamma_3 + \Gamma_4 \gtrsim \Omega_c^2/\Gamma_2$), demonstrating robustness against different fitting choices. When $\Gamma_{3,4}$ become relatively large, the MW Rabi frequency extracted from model fits to high-rate data can show a slight deviation relative to that obtained from low-rate data. This deviation reflects model-dependent lineshape distortion, as none of the parameter choices fully reproduce the observed spectra.

To characterize the full 3D MW field, we vary its frequency and selectively bring the σ^{+} , π , or σ^{-} -polarized components on resonance. As such, we perform three separate sets of spectroscopic measurements to extract the MW electric field amplitude of the $\{\sigma^+, \pi, \sigma^-\}$ polarization (data for π and σ^- polarization presented in Supplementary Part 2). The extracted field amplitudes are $\{1.30(2), 1.19(1), 0.74(1)\}$ mV/cm from the AT splitting and $\{1.25(1), 1.13(1), 0.67(1)\}$ mV/cm from the linear model fits. Since the MW source power and the experimental setup are otherwise identical, these three po-

larization components simultaneously exist at the atom position. Furthermore, we observe no meaningful difference in probe-rate dependence among the spectra of the three polarizations, despite their different interaction coefficients. We verify that our model predictions are insensitive to the values of the coefficients.

Since no spectral shifts are observed, the unconditional model (black solid lines in Fig. 4(a-c)) clearly deviates from our data. Surprisingly, the dephasing model (red dashed lines in Fig. 4(a-c)), while insufficient to explain our three-level EIT data, captures the observed features here. Moreover, it predicts detuning-dependent Rydberg decoherence (Fig. 4(d-f)) such that it increases Γ_3 and Γ_4 to comparable values with increasing probe rate, while still capturing the low probe transmission between the two peaks, thereby resolving the apparent inconsistency in the linear-model fits. If this model is indeed the correct underlying description, it will accurately capture the full lineshape and enable reliable fitting in the deep nonlinear regime. Moreover, another widely used approach to extract the MW Rabi frequency fixes all fields at resonance and performs an atomic superheterodyne measurement [36–38], which may likewise require corrections for Rydberg-induced nonlinearity.

DISCUSSION

In conclusion, we have taken the initial steps to experimentally investigate the nonlinear three-level and four-level EIT spectroscopy arising from Rydberg-Rydberg interactions. In the three-level EIT system, to the best of our knowledge, we are the first to observe interaction-induced peak shifts. The four-level system is particularly relevant in the context of cold-atom MW sensing. The onset of nonlinearity occurs at significantly lower probe rates in the presence of MW fields, manifesting as en-

hanced Rydberg decoherence, without discernible spectral peak shifts. This implies that optimal sensing performance may be achieved in a nonlinear regime, trading peak broadening for reduced photonic and atomic shot noise. Since AT splitting determines MW Rabi frequency solely from spectral peak positions, the extracted values are robust against the nonlinearity. For methods sensitive to lineshapes, moderate broadening does not compromise accuracy; however, a model that properly incorporates lineshape distortion may be required to operate reliably in the deep nonlinear regime.

From the many-body physics point of view, at present, there is no clear consensus in the literature. We compare three representative models, which make qualitatively different predictions. The conditional model is the only one that captures both peak shifts and reductions in peak height when photon-photon interactions increase, which agrees with our three-level EIT observations. In addition, its underlying physical picture is well motivated. We expect that, when properly extended to the four-level system, the conditional model has the potential to account for the full set of experimental observations.

Nevertheless, to our surprise, the dephasing model agrees with our four-level data, particularly capturing the spectroscopic features through its detuning-dependent Rydberg dephasing. It would therefore be valuable to identify the deeper physical reasons that justify this agreement and to delineate the conditions under which the model remains valid. Compared with the conditional model, it has the advantage of conceptual and computational simplicity.

In the future, we will apply a small bias magnetic field such that all the Rydberg Zeeman levels are mixed. In that case, we can extract the electric field amplitudes of all three MW polarizations from a single spectroscopic measurement, without varying the MW frequency or other experimental conditions to individually bring each polarization component on resonance. This approach is also sensitive to the relative phases between different polarization components. Based on our observations in the isolated four-level system, we anticipate that operating in moderate nonlinear regime could increase probe counts without introducing systematic bias, though this remains to be verified experimentally.

METHODS

Spectral fits

All fits are performed using the `curve_fit` function of `scipy.optimize` python package applied to the linear model, where Rydberg-mediated interactions would appear as probe-rate-dependent $\Gamma_{3,4}$ (Rydberg decoherence) and $\Delta_{p,c,m}$ (peak shifts). In the following, we provide analytical solutions for ρ_{ij} and Σ_{ij} at low-probe-rate limit to facilitate understanding, while all fits and model simulations are carried out numerically by solving the master equations.

Three-level EIT We fit spectra from probe frequency scans in a three-level system (Fig. 2) using Eqs. 1 and 2,

with no interaction-induced substitutions and $\Omega_m = 0$. At the low-probe-rate limit, the numerical result asymptotically approaches

$$\rho_{21} = -\frac{i|\Omega_p|}{(\Gamma_2 - 2i\Delta_p) + |\Omega_c|^2/(\Gamma_3 - 2i\delta_2)} \quad (5)$$

The fitted control Rabi frequency at the lowest probe rate is $\Omega_c/(2\pi) = 2.74(5)$ MHz. This value of Ω_c is kept fixed when fitting the higher-rate data. The fitted Γ_3 at all rates are plotted in Fig. 1(c). The fitted probe resonance frequency is used to define their own $\Delta_p = 0$ and shift each spectrum accordingly. In practice, all rates agree within 40 kHz. The fitted $-\Delta_c$ reflects the rate-dependent peak position. In Fig. 1(d), we instead determine the peak position by Gaussian fitting data within $\Delta_p/(2\pi) \in [-2, 2]$ MHz. Peak positions determined in this manner statistically agree with the fitted $-\Delta_c$ while having smaller uncertainty. OD across all rates, except the highest one, agrees within 0.017. The highest rate data has an OD scaled by a factor of 0.76, which we attribute to atom loss from the probing region due to momentum kicks.

In principle, probe Rabi frequency Ω_p can be estimated from the inferred probe rate R_p , together with the probe beam waist. In reality, this method can be inaccurate due to the uncertainty in the actual beam waist and its position relative to the atoms. If we enter the measured values, neither the linear nor the nonlinear models can capture the observed absorption baselines. Therefore, all fits and models in this paper use Ω_p values calculated from the measured probe beam waist ($1/e^2$ radius of 3.7 μm) and scaled down by a factor of 1.6, representing a global uncertainty likely associated with the effective probe size at the atom position. Notably, the control beam shows a similar scaling factor of 1.4 (calculated from its $1/e^2$ radius of 6.8 μm vs the fitted Ω_c).

All models in Fig. 2 share the same input parameters from fitting the lowest-probe-rate data: $\Omega_c/(2\pi) = 2.744$ MHz, $\Delta_c/(2\pi) = 0.02$ MHz, OD = 0.404 (reduced to 0.309 for the highest-rate spectrum), and $\Omega_p/(2\pi) = 0.0887$ MHz at the lowest rate (higher-rate model simulations scaled based on the measured probe rate). For the dephasing model, the interaction-induced $\Gamma_3/(2\pi)$ is added to a base value of 20 kHz. For conditional and unconditional models, $\Gamma_3/(2\pi) = 20$ and 200 kHz, respectively. The number of atoms in each SA, $n_{\text{SA}} = \varrho V_b$, required by all models is derived from the atomic density ϱ , control Rabi frequency Ω_c and the van der Waals coefficient $C_6^{33}/(2\pi) = 169$ GHz (μm)⁶ [39]. Given the parameters here, $n_{\text{SA}} = 46$.

Four-level MW EIT At a large bias magnetic field, we can isolate different four-level systems by varying the MW frequency to selectively bring the σ^+ -, π -, or σ^- -polarized MW electric field component on resonance. By performing three separate spectroscopic measurements, each tuned to a different transition, and fitting the linear model, we extract $\{E_+, E_0, E_-\} = \{1.25(1), 1.13(1), 0.67(1)\}$ mV/cm,

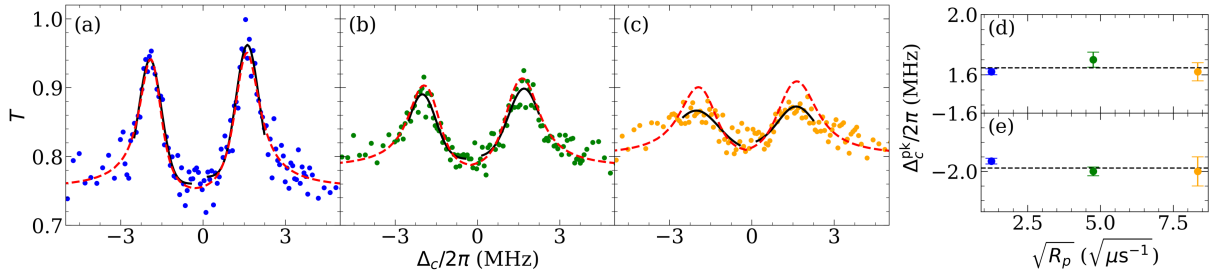


FIG. 5. Nonlinearity in a four-level system at larger probe Rabi frequency. Panels (a-c) are the measured MW EIT spectra vs control detuning with the probe rate $R_p = \{1.6, 22.6, 70.5\} \mu\text{s}^{-1}$ for the {blue, green, orange} colors. $\Omega_c/(2\pi) = 3.19(8) \text{ MHz}$ and $\Omega_m/(2\pi) = 3.45(3) \text{ MHz}$ are extracted through the fit result of (a) from the linear model with independent Γ_3 and Γ_4 . The red dashed lines are the dephasing model, and the black solid lines are Gaussian fits to each peak, from which the peak position Δ_c^{pk} are extracted and plotted in panel (d) (right peaks) and (e) (left peaks).

corresponding to Rabi frequencies $\{\Omega_+, \Omega_0, \Omega_-\}/(2\pi) = \{2.04(2), 2.61(3), 1.88(3)\} \text{ MHz}$ of $|3_{-1/2}\rangle \leftrightarrow \{|4_{-3/2}\rangle, |4_{-1/2}\rangle, |4_{1/2}\rangle\}$ transitions. The fit parameters are $\{\Delta_m, \Omega_m, \Omega_c, \Gamma_3, \Gamma_4, \text{OD}\}$, along with control resonance frequency. We set $\Delta_p = 0$ from a three-level EIT probe-frequency scan in the low probe rate limit, where Rydberg-Rydberg interactions are negligible. The fitted control resonance frequency determines $\Delta_c = 0$ and typically differs by less than $2\pi \times 0.2 \text{ MHz}$ from its independently determined value from three-level EIT spectra. Ω_p is converted from probe rate in the same manner as for the three-level spectra.

The fitted control Rabi frequency at the lowest probe rate in Fig. 3 is $\Omega_c/(2\pi) = 2.76(6) \text{ MHz}$ and is kept fixed when fitting data at higher probe rates. $\{\Delta_m, \Omega_m, \Omega_c\}$ are input parameters to the dephasing and unconditional models presented in Fig. 4. The effective cloud length $L = 64.8 \mu\text{m}$ is kept fixed for all model simulations in this study, while the atomic number density ϱ , and therefore n_{SA} , is varied to account for different OD. Additionally, R_b also varies slightly because different datasets have different Ω_c .

Beyond the probe rate that shows a similar peak reduction to the three-level system, we measure at even higher probe rate (Fig. 5), up to the highest probe rate used in Fig. 1. We observe a similar loss of atoms, with a remaining fraction of 0.76 at the highest probe rate relative to the lowest probe rate, which is accounted for in the model by varying ϱ . The Gaussian-fit results show that we do not observe any spectral shift at this high rate within an uncertainty of 0.1 MHz. This supports that the shifts observed in Fig. 1 are unlikely to be caused by effects associated with momentum kicks.

Interaction coefficients

In addition to C_6^{33} , we also need $C_6^{44}/(2\pi) = -370 \text{ GHz } (\mu\text{m})^6$ [39] and the interaction coefficients between levels $|3_{-1/2}\rangle$ and $|4_{1/2}\rangle$. As shown in Fig. 6, the pair potential exhibits both shifts and splitting. As a result, we jointly fit the two branches with the functions $C_6^{34}/r^6 \pm C_3^{34}/r^3$, where the upper (lower) branch corresponds to the positive (negative) sign, and ob-

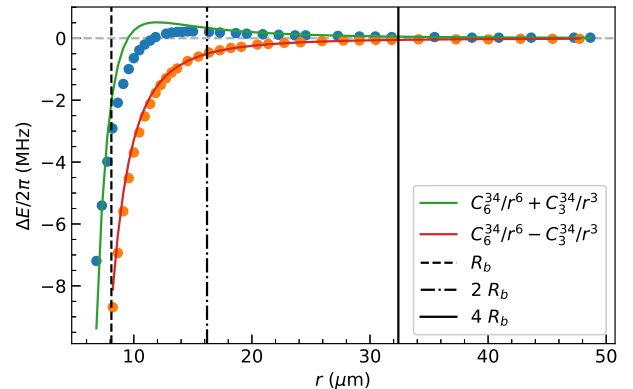


FIG. 6. Interaction energy ΔE vs. interatomic distance r for the $|3_{-1/2}4_{1/2}\rangle$ pairstate. C_6^{34} and C_3^{34} are extracted from a simultaneous fit of the upper (blue) and the lower (orange) branches of the interaction potential obtained from the software `PairInteraction` [40]. The interatomic axis is aligned with the quantization axis ($\theta = 0$) and $B = 15.8 \text{ G}$.

tain $C_6^{34}/(2\pi) = -1517 \text{ GHz } (\mu\text{m})^6$ and $C_3^{34}/(2\pi) = 1.768 \text{ GHz } (\mu\text{m})^3$. C_6^{44} , C_6^{34} and C_3^{34} are all evaluated when the interatomic axis is aligned with the quantization axis, i.e., $\theta = 0$.

Model descriptions

We introduce the zero and first-order collective states $|1_{\text{SA}}\rangle = |1_1, 1_2, \dots, 1_{n_{\text{SA}}}\rangle$, $|2_{\text{SA}}\rangle = \frac{1}{\sqrt{n_{\text{SA}}}} \sum_{j=1}^{n_{\text{SA}}} |1_1, 1_2, \dots, 2_j, \dots, 1_{n_{\text{SA}}}\rangle$, $|3_{\text{SA}}\rangle = \frac{1}{\sqrt{n_{\text{SA}}}} \sum_{j=1}^{n_{\text{SA}}} |1_1, 1_2, \dots, 3_j, \dots, 1_{n_{\text{SA}}}\rangle$, and $|4_{\text{SA}}\rangle = \frac{1}{\sqrt{n_{\text{SA}}}} \sum_{j=1}^{n_{\text{SA}}} |1_1, 1_2, \dots, 4_j, \dots, 1_{n_{\text{SA}}}\rangle$. With these collective states as the basis states, we have $\varrho_{33} \approx \varrho_{\text{SA}} \Sigma_{33}$, $\varrho_{44} \approx \varrho_{\text{SA}} \Sigma_{44}$, and $\varrho_{34} \approx \varrho_{\text{SA}} \Sigma_{34}$, where $\varrho_{\text{SA}} = V_b^{-1}$ is the SA number density. Assuming the MW on resonance, and the Rydberg decoherence is negligible,

i.e. $\Delta_m = \Gamma_3 = \Gamma_4 = 0$, we have

$$\Sigma_{33} = \frac{n_{\text{SA}} |\Omega_c|^2 |\tilde{\Omega}_p|^2 (2\delta_2)^2}{|A|^2 + n_{\text{SA}} |\Omega_c|^2 |\tilde{\Omega}_p|^2 \left[(2\delta_2)^2 + |\Omega_m|^2 \right]} \quad (6a)$$

$$\Sigma_{44} = \frac{n_{\text{SA}} |\Omega_c|^2 |\tilde{\Omega}_p|^2 |\Omega_m|^2}{|A|^2 + n_{\text{SA}} |\Omega_c|^2 |\tilde{\Omega}_p|^2 \left[(2\delta_2)^2 + |\Omega_m|^2 \right]} \quad (6b)$$

$$\Sigma_{34} = \frac{n_{\text{SA}} |\Omega_c|^2 |\tilde{\Omega}_p|^2 |\Omega_m| (2\delta_2)}{|A|^2 + n_{\text{SA}} |\Omega_c|^2 |\tilde{\Omega}_p|^2 \left[(2\delta_2)^2 + |\Omega_m|^2 \right]} \quad (6c)$$

where $A = (2\delta_2) [(2\Delta_p - i\Gamma_2)(2\delta_2) - |\Omega_c|^2] - (2\Delta_p - i\Gamma_2)|\Omega_m|^2$. For all models, we obtain the three-level EIT results by setting $\Omega_m = 0$.

The mean-field interactions are obtained by integrating over a spherical shell volume between radii R and R' :

$$s_{33} = \Sigma_{33} \varrho_{\text{SA}} C_6^{33} \int_{R < r < R'} d^3 r \frac{1}{r^6} \quad (7a)$$

$$s_{44} = \Sigma_{44} \varrho_{\text{SA}} C_6^{44} \int_{R < r < R'} d^3 r \frac{|3 \cos^2 \theta - 1|}{2r^6} \quad (7b)$$

$$s_{34} = \Sigma_{44} \varrho_{\text{SA}} C_6^{34} \int_{R < r < R'} d^3 r \frac{|3 \cos^2 \theta - 1|}{2r^6} \quad (7c)$$

$$s_{43} = \Sigma_{33} \varrho_{\text{SA}} C_6^{34} \int_{R < r < R'} d^3 r \frac{|3 \cos^2 \theta - 1|}{2r^6} \quad (7d)$$

$$e_{34} = |\Sigma_{34}| \varrho_{\text{SA}} C_3^{34} \int_{R < r < R'} d^3 r \frac{|3 \cos^2 \theta - 1|}{2r^3} \quad (7e)$$

where we have approximated the angular dependence of the anisotropic RydbergRydberg interactions as $\frac{|3 \cos^2 \theta - 1|}{2}$.

Conditional SA model The conditional probe-transition coherence ρ_{21} is

$$\rho_{21} = \Sigma_{33} \rho_{21}^{\text{2-level}} + (1 - \Sigma_{33}) \rho_{21}^{\text{MF}} \quad (8)$$

with

$$\rho_{21}^{\text{2-level}} = -\frac{i|\Omega_p|}{\Gamma_2 - 2i\Delta_p} \quad (9a)$$

$$\rho_{21}^{\text{MF}} = -\frac{i|\Omega_p|}{(\Gamma_2 - 2i\Delta_p) + |\Omega_c|^2 / [\Gamma_3 - 2i(\delta_2 - s_{33})]} \quad (9b)$$

We consider 1D SA chain and divide the propagation length L into $L/(2R_b)$ intervals. The input coherent probe field has local probe field intensity correlation function $g^{(2)}(z = 0) = 1$. At each SA, we evaluate $\Sigma_{33}(z)$ (Eq. 6(a)) by weighting the local probe intensity $|\Omega_p(z)|^2$ with $g^{(2)}(z)$, i.e. $|\tilde{\Omega}_p(z)|^2 \rightarrow |\Omega_p(z)|^2 g^{(2)}(z)$. We perform Monte Carlo sampling accordingly: with probability Σ_{33} , $n_{33} = 1$; and with probability $1 - \Sigma_{33}$, $n_{33} = 0$. To differentiate from the ensemble-averaged population Σ_{33} , we introduce a binary stochastic variable n_{33} to represent the Monte Carlo outcome. The mean-field interactions

(Eq. 7) are evaluated by setting $g^{(2)} = 1$. The results are used to calculate

$$\alpha(z) = n_{33}(z) \alpha^{\text{2-level}} + (1 - n_{33}(z)) \alpha^{\text{MF}}(z) \quad (10)$$

where α denotes the polarizability, with $\alpha^{\text{2-level}} = -\rho_{21}^{\text{2-level}} \Gamma_2 / |\Omega_p|$ and $\alpha^{\text{MF}} = -\rho_{21}^{\text{MF}} \Gamma_2 / |\Omega_p|$. The following equations are used to determine $|\Omega_p(z)|^2$ and $g^{(2)}(z)$ for the next SA step, using the polarizability in Eq. 10:

$$\partial_z (|\Omega_p|^2) = -\kappa(z) |\Omega_p|^2 \text{Im}[\alpha(z)] \quad (11a)$$

$$\partial_z g_p^{(2)}(z) = -\kappa(z) n_{33}(z) \text{Im}[\alpha^{\text{2-level}} - \alpha^{\text{MF}}(z)] g_p^{(2)}(z) \quad (11b)$$

where $\kappa(z) = 2\varrho\omega_p |\wp_{12}|^2 / (\hbar\epsilon_0 c \Gamma_2)$. Here, \wp_{12} is the dipole moment of the $|1\rangle \leftrightarrow |2\rangle$ transition, and ω_p is the corresponding transition angular frequency.

Unconditional SA model In this model, $\rho_{21} = \rho_{21}^{\text{MF}}$ unconditionally. For the three-level EIT system, it takes the same form as Eq. 9(b); for the four-level MW EIT system, it is

$$\rho_{21} = -\frac{i|\Omega_p|}{(\Gamma_2 - 2i\Delta_p) + \frac{|\Omega_c|^2(\Gamma_4 - 2i\delta'_3)}{|\Omega_m|^2 + (e_{34})^2 + (\Gamma_3 - 2i\delta'_2)(\Gamma_4 - 2i\delta'_3)}} \quad (12)$$

with $\delta'_2 = \Delta_p + \Delta_c - s_{33} - s_{34}$ and $\delta'_3 = \Delta_p + \Delta_c + \Delta_m - s_{44} - s_{43}$. When modeling the four-level system, because of the slow spatial decay of the C_3^{34} interaction, in Eq. 7 we set the upper limit of the integration range to $R' = L/2$. Due to the differences in the interaction strengths, each integral has its own lower cutoff R , set by equating the corresponding interaction to $\Omega_c^2/(2\Gamma_2)$. $\Gamma_{3,4}/(2\pi) = 0.2$ MHz is included in the model to match our measurements at the lowest probe rates.

Dephasing model In this model, the effects of interactions are included as increased decoherence rather than shifts:

$$\rho_{21} = -\frac{i|\Omega_p|}{(\Gamma_2 - 2i\Delta_p) + \frac{|\Omega_c|^2(\Gamma'_4 - 2i\delta_3)}{|\Omega_m|^2 + (\Gamma'_3 - 2i\delta_2)(\Gamma'_4 - 2i\delta_3)}} \quad (13)$$

with $\Gamma'_3 = 2\pi \times 20$ kHz + $\sqrt{\text{Var}_{33}}$ + $\sqrt{\text{Var}_{34}^s}$ + $\sqrt{\text{Var}_{34}^e}$, $\Gamma'_4 = 2\pi \times 20$ kHz + $\sqrt{\text{Var}_{44}}$ + $\sqrt{\text{Var}_{43}^s}$ + $\sqrt{\text{Var}_{34}^e}$, and

$$\text{Var}_{33} = \Sigma_{33} \varrho_{\text{SA}} \int_{R < r < R'} d^3 r \left[\frac{C_6^{33}}{r^6} - \frac{\overline{C_6^{33}}}{r^6} \right]^2 \quad (14a)$$

$$\text{Var}_{44} = \Sigma_{44} \varrho_{\text{SA}} \int_{R < r < R'} d^3 r \left[\frac{C_6^{44}(\theta)}{r^6} - \frac{\overline{C_6^{44}(\theta)}}{r^6} \right]^2 \quad (14b)$$

$$\text{Var}_{34}^s = \Sigma_{44} \varrho_{\text{SA}} \int_{R < r < R'} d^3 r \left[\frac{C_6^{34}(\theta)}{r^6} - \frac{\overline{C_6^{34}(\theta)}}{r^6} \right]^2 \quad (14c)$$

$$\text{Var}_{43}^s = \Sigma_{33} \varrho_{\text{SA}} \int_{R < r < R'} d^3 r \left[\frac{C_6^{34}(\theta)}{r^6} - \frac{\overline{C_6^{34}(\theta)}}{r^6} \right]^2 \quad (14d)$$

$$\text{Var}_{34}^e = |\Sigma_{34}| \varrho_{\text{SA}} \int_{R < r < R'} d^3 r \left[\frac{C_3^{34}(\theta)}{r^3} - \frac{\overline{C_3^{34}(\theta)}}{r^3} \right]^2 \quad (14e)$$

where

$$\frac{\overline{C_6^{33}}}{r^6} = \frac{1}{\mathcal{N}} \int_{R < r < R'} d^3 r \frac{C_6^{33}}{r^6} \quad (15a)$$

$$\frac{\overline{C_6^{ij}(\theta)}}{r^6} = \frac{1}{\mathcal{N}} \int_{R < r < R'} d^3 r \frac{C_6^{ij}(\theta)}{r^6} \quad (15b)$$

$$\frac{\overline{C_3^{34}(\theta)}}{r^3} = \frac{1}{\mathcal{N}} \int_{R < r < R'} d^3 r \frac{C_3^{34}(\theta)}{r^3} \quad (15c)$$

with $C_6^{ij}(\theta) = C_6^{ij} \frac{|3\cos^2 \theta - 1|}{2}$, $C_3^{34}(\theta) = C_3^{34} \frac{|3\cos^2 \theta - 1|}{2}$, and the normalization factor $\mathcal{N} = \int_{R < r < R'} d^3 r = \frac{4\pi}{3} (R'^3 - R^3)$. The integration range cutoffs R and R' are set in the same manner as for the unconditional model. Additionally, $\tilde{\Omega}_p = \Omega_p$ for both models.

DATA AVAILABILITY

The data and code that support the findings of this study are openly available in Zenodo at <https://doi.org/10.5281/zenodo.18560777>.

ACKNOWLEDGMENTS

We thank Profs. Chen-Lung Hung and Jonathan D. Hood for loaning us equipment. We are grateful for valuable discussions with Chen-Lung Hung. This work was supported by Purdue startup fund and AFOSR Grant FA9550-22-1-0327.

Supplementary Information:
Nonlinear optical spectra from Rydberg-mediated photon-photon interactions

PART 1. DISCREPANCY BETWEEN AT-SPLITTING AND FITTED MICROWAVE RABI FREQUENCY

In this section, we report the discrepancy between the given microwave Rabi frequency Ω_m and the corresponding Autler-Townes (AT) splitting Δ_{AT} , which is extracted from the peak positions of the two maxima in the simulated spectra for different values of Γ_3 and Γ_4 . The fixed parameters used in the simulations are $\{\Delta_m, \Omega_m, \Omega_c\}/(2\pi) = \{0, 2.04, 2.76\}$ MHz and OD = 0.347, taken from the fit results of Fig. 3(e) in the main text, except that Δ_m is set to zero. The spectra are simulated over the ranges $\Delta_c/(2\pi) \in [-\Omega_m/(4\pi) - 0.5, -\Omega_m/(4\pi) + 0.5]$ MHz and $\Delta_c/(2\pi) \in [\Omega_m/(4\pi) - 0.5, \Omega_m/(4\pi) + 0.5]$ MHz, using 2000 sampling points for each interval, corresponding to a frequency resolution of 0.5 kHz.

Fig. S7(a) clearly shows that, within our operating regime, a systematic discrepancy exists between the Δ_{AT} the Ω_m used in the model. The simulated discrepancy $((\Delta_{\text{AT}} - \Omega_m)/(2\pi))$ is +0.04 MHz, which agrees with the value reported in the main text (+0.07(4) MHz) within the experimental uncertainty. In contrast, when the microwave Rabi frequency is increased by a factor of five (Fig. S7(b)), the peak separation becomes much larger than the linewidth. In this regime the two resonances are well resolved, the lineshape approaches the ideal AT picture, and the discrepancy vanishes.

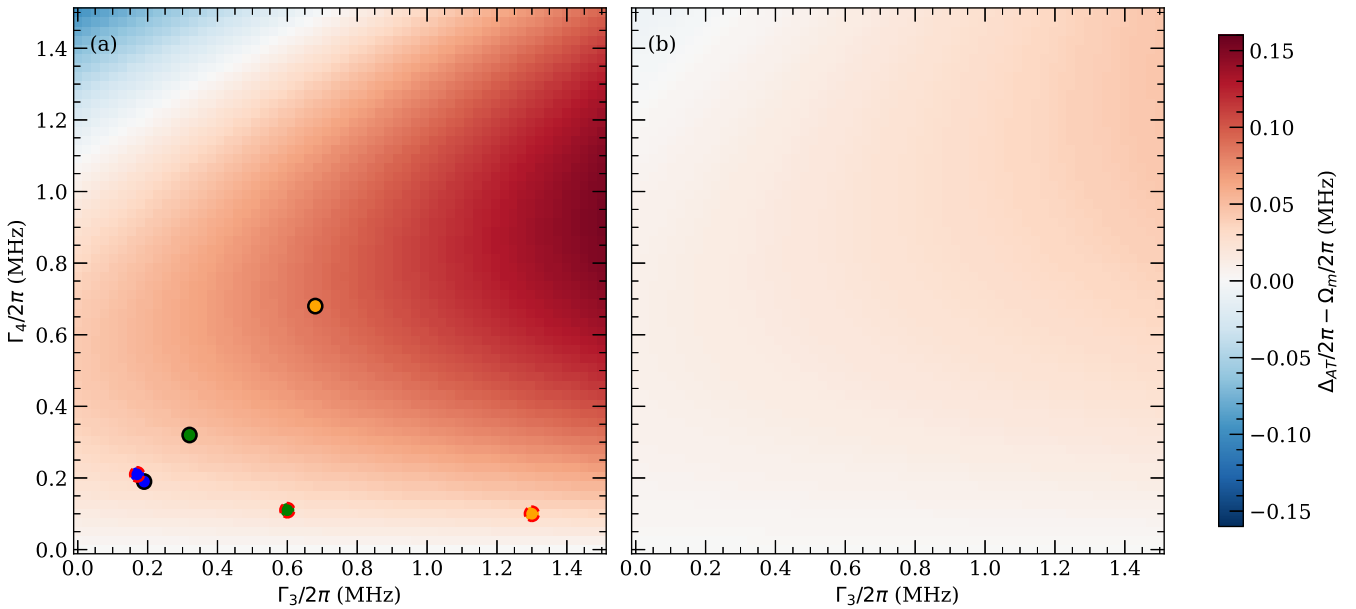


FIG. S7. AT-splitting and curvefit result discrepancy. (a) Calculated discrepancy with the fit results of the data in Fig. 3(e) in the main text except Δ_m is set to be 0 as a function of Γ_3 and Γ_4 . Colored markers correspond to the three representative parameter sets with the red dashed and black solid marker edges denote the two fitting strategies within the same linear model, as shown in Fig. 3(e)(g) of the main text. (b) Same calculation as in (a) but with the Ω_m increased by a factor of five.

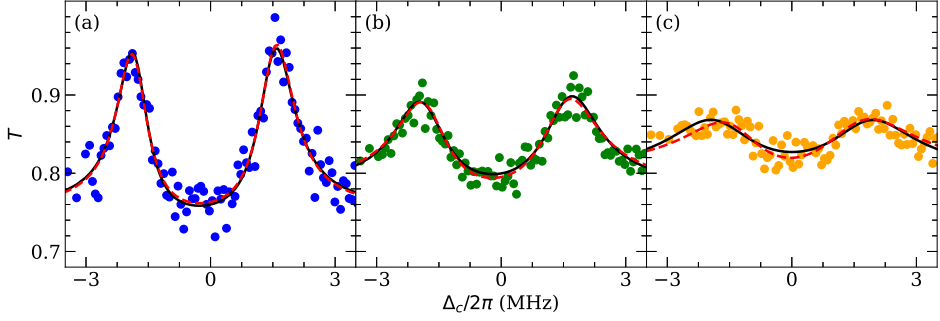
PART 2. FIT RESULTS FOR FIG. 5 AND ADDITIONAL TRANSITIONS


FIG. S8. Fit results from the linear model for the data shown in Fig. 5 of the main text. In panels (a-c), the red dashed lines have independent Γ_3 and Γ_4 , with fitted values $\Gamma_3/(2\pi) = \{0.0(1), 1.1(2), 2.5(3)\}$ MHz and $\Gamma_4/(2\pi) = \{0.3(1), 0.4(1), 0.8(2)\}$ MHz. The black solid lines enforces $\Gamma_3 = \Gamma_4$, with fitted values $\Gamma_{3,4}/(2\pi) = \{0.16(3), 0.74(5), 1.6(1)\}$ MHz.

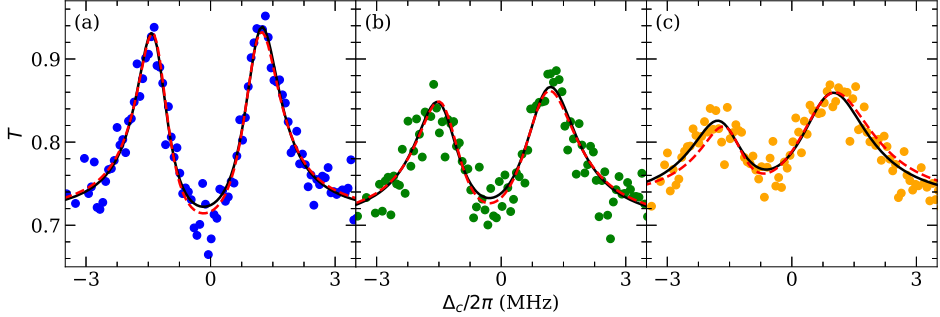


FIG. S9. Fit results from the linear model for the π transition data. In panels (a-c), the red dashed lines have independent Γ_3 and Γ_4 , with fitted values $\Gamma_3/(2\pi) = \{0.4(1), 0.9(2), 1.2(1)\}$ MHz and $\Gamma_4/(2\pi) = \{0.04(8), 0.5(1), 0.7(2)\}$ MHz. The black solid line enforces $\Gamma_3 = \Gamma_4$, with fitted values $\Gamma_{3,4}/(2\pi) = \{0.21(3), 0.66(5), 1.00(6)\}$ MHz.

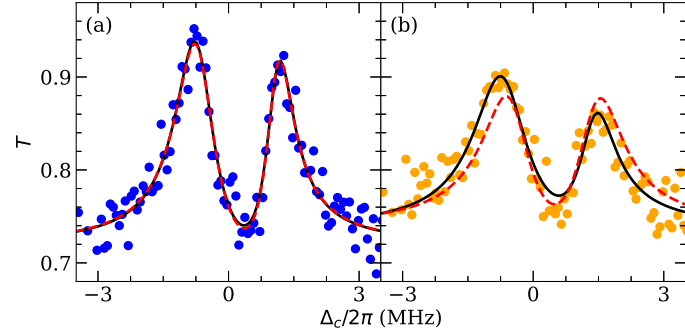


FIG. S10. Fit results from the linear model for the σ^- transition data. In panels (a-b), the red dashed lines have independent Γ_3 and Γ_4 , with fitted values $\Gamma_3/(2\pi) = \{0.27(7), 0.8(2)\}$ MHz and $\Gamma_4/(2\pi) = \{0.18(6), 0.3(1)\}$ MHz. The black solid lines enforces $\Gamma_3 = \Gamma_4$, with fitted values $\Gamma_{3,4}/(2\pi) = \{0.22(2), 0.54(4)\}$ MHz.

[1] L. Henriet, L. Beguin, A. Signoles, T. Lahaye, A. Browaeys, G.-O. Reymond, and C. Jurczak, Quantum computing with neutral atoms, *Quantum* **4**, 327 (2020).

- [2] T. Graham, Y. Song, J. Scott, C. Poole, L. Phuttitarn, K. Jooya, P. Eichler, X. Jiang, A. Marra, B. Grinkemeyer, *et al.*, Multi-qubit entanglement and algorithms on a neutral-atom quantum computer, *Nature* **604**, 457 (2022).
- [3] J. Muniz, M. Stone, D. Stack, M. Jaffe, J. Kindem, L. Wadleigh, E. Zalys-Geller, X. Zhang, C.-A. Chen, M. Norcia, *et al.*, High-fidelity universal gates in the 171 yb ground-state nuclear-spin qubit, *PRX Quantum* **6**, 020334 (2025).
- [4] M. Saffman, T. G. Walker, and K. Mølmer, Quantum information with rydberg atoms, *Reviews of modern physics* **82**, 2313 (2010).
- [5] D. E. Chang, V. Vuletić, and M. D. Lukin, Quantum nonlinear opticsphoton by photon, *Nature Photonics* **8**, 685 (2014).
- [6] C. S. Adams, J. D. Pritchard, and J. P. Shaffer, Rydberg atom quantum technologies, *Journal of Physics B: Atomic, Molecular and Optical Physics* **53**, 012002 (2019).
- [7] Q.-Y. Liang, A. V. Venkatramani, S. H. Cantu, T. L. Nicholson, M. J. Gullans, A. V. Gorshkov, J. D. Thompson, C. Chin, M. D. Lukin, and V. Vuletić, Observation of three-photon bound states in a quantum nonlinear medium, *Science* **359**, 783 (2018).
- [8] D. P. Ornelas-Huerta, A. N. Craddock, E. A. Goldschmidt, A. J. Hachtel, Y. Wang, P. Bienias, A. V. Gorshkov, S. L. Rolston, and J. V. Porto, On-demand indistinguishable single photons from an efficient and pure source based on a rydberg ensemble, *Optica* **7**, 813 (2020).
- [9] T. Stoltz, H. Hegels, M. Winter, B. Röhr, Y.-F. Hsiao, L. Husel, G. Rempe, and S. Dürr, Quantum-logic gate between two optical photons with an average efficiency above 40%, *Physical Review X* **12**, 021035 (2022).
- [10] J. Vaneecloo, S. Garcia, and A. Ourjoumtsev, Intracavity rydberg superatom for optical quantum engineering: Coherent control, single-shot detection, and optical π phase shift, *Physical Review X* **12**, 021034 (2022).
- [11] R. Bekenstein, I. Pikovski, H. Pichler, E. Shahmoon, S. F. Yelin, and M. D. Lukin, Quantum metasurfaces with atom arrays, *Nature Physics* **16**, 676 (2020).
- [12] E. Oh, X. Lai, J. Wen, and S. Du, Distributed quantum computing with photons and atomic memories, *Advanced Quantum Technologies* **6**, 2300007 (2023).
- [13] A. Grankin, P. Guimond, D. Vasilyev, B. Vermersch, and P. Zoller, Free-space photonic quantum link and chiral quantum optics, *Physical Review A* **98**, 043825 (2018).
- [14] D. H. Meyer, Z. A. Castillo, K. C. Cox, and P. D. Kunz, Assessment of rydberg atoms for wideband electric field sensing, *Journal of Physics B: Atomic, Molecular and Optical Physics* **53**, 034001 (2020).
- [15] N. Schlossberger, N. Prajapati, S. Berweger, A. P. Rotunno, A. B. Artusio-Glimpse, M. T. Simons, A. A. Sheikh, E. B. Norrgard, S. P. Eckel, and C. L. Holloway, Rydberg states of alkali atoms in atomic vapour as si-traceable field probes and communications receivers, *Nature Reviews Physics* **6**, 606 (2024).
- [16] H. Zhang, Y. Ma, K. Liao, W. Yang, Z. Liu, D. Ding, H. Yan, W. Li, and L. Zhang, Rydberg atom electric field sensing for metrology, communication and hybrid quantum systems, *Science Bulletin* **69**, 1515 (2024).
- [17] J. Kitching, J. P. Shaffer, and D. Budker, Atom-based quantum sensing of electromagnetic fields, *Optica* **12**, 2008 (2025).
- [18] H.-T. Tu, K.-Y. Liao, H.-L. Wang, Y.-F. Zhu, S.-Y. Qiu, H. Jiang, W. Huang, W. Bian, H. Yan, and S.-L. Zhu, Approaching the standard quantum limit of a rydberg-atom microwave electrometer, *Science Advances* **10**, 10.1126/sciadv.ads0683 (2024).
- [19] R. Duverger, A. Bonnin, R. Granier, Q. Marolleau, C. Blanchard, N. Zahzam, Y. Bidel, M. Cadoret, A. Bresson, and S. Schwartz, Metrology of microwave fields based on trap-loss spectroscopy with cold rydberg atoms, *Physical Review Applied* **22**, 044039 (2024).
- [20] M. J. Jamieson, K. J. Weatherill, C. S. Adams, R. K. Hanley, N. Alves, and J. Keaveney, Continuous time ultra-high frequency (uhf) sensing using ultra-cold rydberg atoms, *arXiv preprint arXiv:2504.00212* (2025).
- [21] K.-Y. Liao, H.-T. Tu, S.-Z. Yang, C.-J. Chen, X.-H. Liu, J. Liang, X.-D. Zhang, H. Yan, and S.-L. Zhu, Microwave electrometry via electromagnetically induced absorption in cold rydberg atoms, *Physical Review A* **101**, 053432 (2020).
- [22] F. Zhou, F. Jia, X. Liu, Y. Yu, J. Mei, J. Zhang, F. Xie, and Z. Zhong, Improving the spectral resolution and measurement range of quantum microwave electrometry by cold rydberg atoms, *Journal of Physics B: Atomic, Molecular and Optical Physics* **56**, 025501 (2023).
- [23] P. L. Ocola, I. Dimitrova, B. Grinkemeyer, E. Guardado-Sánchez, T. Đorđević, P. Samutpraphoot, V. Vuletić, and M. D. Lukin, Control and entanglement of individual rydberg atoms near a nanoscale device, *Physical Review Letters* **132**, 113601 (2024).
- [24] S. Chen, H. Fukuda, T. Inada, T. Moroi, T. Nitta, and T. Sichanugrist, Quantum enhancement in dark matter detection with quantum computation, *Physical Review Letters* **133**, 021801 (2024).
- [25] J. Shu, B. Xu, and Y. Xu, Eliminating incoherent noise: A coherent quantum approach in multi-sensor dark matter detection, *arXiv preprint arXiv:2410.22413* (2024).
- [26] C. Nill, A. Cabot, A. Trautmann, C. Groß, and I. Lesanovsky, Avalanche terahertz photon detection in a rydberg tweezer array, *Physical Review Letters* **133**, 073603 (2024).
- [27] X. Wang, Y. Wang, and Q.-Y. Liang, Robust rydberg facilitation via rapid adiabatic passage, *arXiv preprint arXiv:2510.01504* (2025).
- [28] M. Gullans, J. Thompson, Y. Wang, Q.-Y. Liang, V. Vuletić, M. D. Lukin, and A. V. Gorshkov, Effective field theory for rydberg polaritons, *Physical review letters* **117**, 113601 (2016).
- [29] T. Peyronel, O. Firstenberg, Q.-Y. Liang, S. Hofferberth, A. V. Gorshkov, T. Pohl, M. D. Lukin, and V. Vuletić, Quantum nonlinear optics with single photons enabled by strongly interacting atoms, *Nature* **488**, 57 (2012).
- [30] J. D. Pritchard, D. Maxwell, A. Gauguet, K. J. Weatherill, M. Jones, and C. S. Adams, Cooperative atom-light interaction in a blockaded rydberg ensemble, *Physical review letters* **105**, 193603 (2010).
- [31] D. Petrosyan, J. Otterbach, and M. Fleischhauer, Electromagnetically induced transparency with rydberg atoms, *Physical*

- review letters **107**, 213601 (2011).
- [32] Z. Vendeiro, J. Ramette, A. Rudelis, M. Chong, J. Sinclair, L. Stewart, A. Urvoy, and V. Vuletić, Machine-learning-accelerated bose-einstein condensation, *Physical Review Research* **4**, 043216 (2022).
- [33] D. Kurdak, Y. Li, P. R. Banner, J. Porto, and S. Rolston, High-fidelity microwave-polarization control in a rydberg-ensemble experiment, *arXiv preprint arXiv:2508.06820* (2025).
- [34] B.-B. Wang, D. Yan, and J.-H. Wu, Enhanced microwave electrometry in weakly interacting rydberg atoms using a modified formula, *Optics Express* **33**, 17026 (2025).
- [35] C. L. Holloway, M. T. Simons, J. A. Gordon, A. Dienstfrey, D. A. Anderson, and G. Raithel, Electric field metrology for si traceability: Systematic measurement uncertainties in electromagnetically induced transparency in atomic vapor, *Journal of Applied Physics* **121** (2017).
- [36] M. Jing, Y. Hu, J. Ma, H. Zhang, L. Zhang, L. Xiao, and S. Jia, Atomic superheterodyne receiver based on microwave-dressed rydberg spectroscopy, *Nature Physics* **16**, 911 (2020).
- [37] J. A. Gordon, M. T. Simons, A. H. Haddab, and C. L. Holloway, Weak electric-field detection with sub-1 hz resolution at radio frequencies using a rydberg atom-based mixer, *Aip Advances* **9** (2019).
- [38] N. Prajapati, A. K. Robinson, S. Berweger, M. T. Simons, A. B. Artusio-Glimpse, and C. L. Holloway, Enhancement of electromagnetically induced transparency based rydberg-atom electrometry through population repumping, *Applied Physics Letters* **119** (2021).
- [39] N. Šibalić, J. D. Pritchard, C. S. Adams, and K. J. Weatherill, Arc: An open-source library for calculating properties of alkali rydberg atoms, *Computer Physics Communications* **220**, 319 (2017).
- [40] S. Weber, C. Tresp, H. Menke, A. Urvoy, O. Firstenberg, H. P. Büchler, and S. Hofferberth, Tutorial: Calculation of rydberg interaction potentials, *Journal of Physics B: Atomic, Molecular and Optical Physics* **50**, 133001 (2017).